Materials Horizons

ROYAL SOCIETY OF CHEMISTRY

COMMUNICATION

View Article Online
View Journal

Cite this: DOI: 10.1039/d5mh01407g

Received 22nd July 2025,
Accepted 5th January 2026

DOI: 10.1039/d5mh01407g

rsc.li/materials-horizons

Core–shell Mg–Ni carbonate supercapacitor materials by concurrent Ni recovery and CO_2 mineralization

Ying Wang, [a] Xueyi Liu, [a] Sebastien N. Kerisit [b] and Young-Shin Jun *[a]

Quickly increasing CO_2 concentrations and rising demands for nickel (Ni) urge us to develop new efficient Ni recovery methods from unconventional resources, such as mafic and ultramafic low-grade ores, while simultaneously reducing CO_2 concentrations. Concurrent CO_2 mineralization and Ni recovery offer great potential for addressing both environmental and resource challenges efficiently. However, the formation of Ni carbonate in the presence of major alkaline earth cations that widely coexist (*i.e.*, Mg) during CO_2 mineralization remains unclear, complicating the product separation and utilization. Here, we investigated the formation of Mg and Ni carbonates at 180 °C and a CO_2 pressure of 100 bar. The results demonstrated that a core–shell structure of Ni–Mg carbonates was formed, where magnesite ($MgCO_3$) constituted the core and gaspéite ($NiCO_3$) formed the shell ($MgCO_3$@$NiCO_3$). This structure arose because magnesite crystallized faster than gaspéite, serving as a substrate that promoted the nucleation of gaspéite, as supported by the thermodynamic calculation of interfacial energies. However, the core–shell structure of Ni and Mg coprecipitates may still hinder the selective recovery of Ni from Mg. To address this challenge, we showed that the $MgCO_3$@$NiCO_3$ product can be directly used as a supercapacitor electrode without further treatment. The cyclic voltammetry (CV) results revealed that the composite had a capacitance comparable to that of pure $NiCO_3$ and a long recyclability. This study provides insights into carbonate mineral coprecipitation, applicable to Ni recovery from sources (*e.g.*, electronic waste and silicate minerals), and introduces novel electrode materials to be used in catalysts and ion batteries, making the overall process more sustainable.

New concepts

CO_2 mineralization is a promising method for capturing and storing CO_2 to mitigate increasing CO_2 concentrations. Simultaneously, the rising demand for critical elements such as nickel (Ni) (used as electrodes for energy storage) and the depletion of high-grade resources underscore the need to recover these elements from their unconventional sources, such as low-grade ores and industrial solid waste. However, the process of carbonation coprecipitation involving both alkaline cations (such as magnesium (Mg)) and critical elements (such as Ni) is not well understood. Furthermore, the additional treatment required to separate Ni from the coprecipitate may result in high energy consumption and potential CO_2 release due to carbonate dissolution. To address these knowledge gaps, we first investigated the coprecipitation of Mg and Ni carbonates. A core–shell structure (denoted as $MgCO_3$@$NiCO_3$) with magnesite ($MgCO_3$) as the core and gaspéite ($NiCO_3$) as the shell was formed. Then, we tested the electrochemical properties of the recovered $MgCO_3$@$NiCO_3$ as an electrode. $MgCO_3$@$NiCO_3$ exhibited excellent capacitance and cycling stability. This research demonstrates great promise for the simultaneous CO_2 mineralization and recovery of critical elements, with potential utilization as a supercapacitor electrode to aid in energy storage.

1. Introduction

Nickel (Ni) and its compounds are extensively utilized across various industries because of their excellent intrinsic properties, including high corrosion resistance, temperature stability, and high electrochemical capacity.[1–3] For instance, Ni is a critical component in producing stainless-steel and nonferrous alloys.[4] Ni is also used in electrodes for rechargeable batteries.[5,6] Ni is a key component for commercial electric vehicles (EVs), comprising 66% of light-duty EV batteries in 2023. The demand for battery-grade nickel is projected to grow by 400% to 600% by 2030, driven by the increasing adoption of EVs under climate-driven scenarios.[7] This highlights the importance of Ni in energy storage and sustainability development. However, due to the extensive use of nickel products, the demand for Ni has greatly increased. Traditional sources of Ni, primarily extracted from sulfide ores, are becoming increasingly depleted.[8] Combined with the growing demand for high-grade ores, this depletion necessitates the extraction of Ni from lower-grade sources, such as silicate-based ores. Conventional methods of Ni extraction—such as pyrometallurgical routes,

[a] Department of Energy, Environmental & Chemical Engineering, Washington University in St. Louis, St. Louis, Missouri, 63130, USA. E-mail: ysjun@seas.wustl.edu; Web: https://encl.engineering.wustl.edu/
[b] Physical and Computational Sciences Directorate, Pacific Northwest National Laboratory, Richland, WA, 99352, USA

hydrometallurgical routes, and the Caron process—require high CO_2 emissions.[9] Therefore, it is imperative to enhance Ni recovery from low-grade ores while simultaneously reducing the carbon footprint of its extraction process.

Alternative Ni resources, such as mafic and ultramafic rocks,[10] mining waste,[11] and electronic waste,[12] have significant potential to achieve concurrent Ni supplementation and CO_2 emission reduction.[13,14] These alternatives not only contain Ni but also include alkaline cations such as magnesium (Mg), which can be utilized as feedstock for CO_2 mineralization. Examples of mafic and ultramafic rocks include olivine and serpentinite, where the Ni content in these rocks varies: olivine typically contains 0.1% to 0.5% Ni by weight (wt),[15] and serpentinite can contain up to 0.36 wt% Ni.[16] Apart from Ni, these rocks are rich in Mg, iron (Fe), and calcium (Ca), making them even more suitable for CO_2 capture. For example, forsterite (Mg_2SiO_4) can dissolve and release Mg ions, which then react with dissolved CO_2 to form magnesium carbonate (Mg-carbonate). This process, known as CO_2 mineralization, effectively captures and stores CO_2.[17] Furthermore, the concentration of Ni in mining-polluted water is 0.66 ppm, while the Mg concentration is 13.26 ppm.[11] Additionally, the concentrations of Ni and Mg in electronic waste leachates are 89 ppm and 0.09 ppm, respectively.[12] The coexistence of Ni and Mg in the above alternatives highlights the importance of studying the coprecipitation of Mg and Ni-containing waste.

The recovery of Ni through carbonation processes has begun to attract growing attention as a potentially efficient and sustainable strategy. For example, CO_2 mineralization and concurrent utilization for nickel conversion from nickel silicates to nickel sulfides demonstrates an integrated approach that couples CO_2 sequestration with the transformation of nickel species.[18] Similarly, carbon mineralization with concurrent critical metal recovery from olivine using a metal-complexing ligand highlights how CO_2 mineralization can be leveraged to simultaneously capture carbon and extract valuable metals from ultramafic minerals.[19] In addition, carbonation and sulfidation of Mg- and Ni-containing solutions provide a mechanistic understanding of the coupled precipitation pathways of Ni-carbonates and Ni-sulfides.[20] These studies collectively underscore the potential of CO_2 mineralization as a dual-function strategy for both CO_2 capture and critical metal recovery.

The nature of Mg- and Ni-containing carbonation products depends on reaction conditions. The formation of Mg-carbonate is influenced by factors such as temperature, CO_2 pressure, supersaturation, and pH.[21,22] At low temperatures and low CO_2 pressure, hydrous magnesium carbonates, such as nesquehonite ($MgCO_3{\cdot}3H_2O$) and hydromagnesite ($(MgCO_3)_4{\cdot}Mg(OH)_2{\cdot}4H_2O$), precipitate first and then transform into the thermodynamically most stable form of Mg-carbonate, magnesite ($MgCO_3$). This occurs because the high dehydration-free energy of Mg^{2+} hinders the direct precipitation of magnesite. Unlike Mg-carbonate, Ni-carbonate formation has been studied less. Hydrous nickel carbonates, such as the hexahydrate form (hellyerite, $NiCO_3{\cdot}6H_2O$) and the hydroxyhydrate form (zaratite, $Ni_3(CO_3)(OH)_4{\cdot}4H_2O$), can form at room temperature.[23] As the temperature increases, nickel bicarbonate (nickel hydrogen carbonate, $Ni(HCO_3)_2$) can form. $Ni(HCO_3)_2$ formation can serve as an intermediate step in dehydrating Ni-carbonates, ultimately leading to anhydrous calcite-type gaspéite ($NiCO_3$).

Among all the polymorphs of Mg-carbonates and Ni-carbonates, the anhydrous rhombohedral *R*3*c* calcite-type structure is the dominant phase under high temperature and high pressure conditions. Magnesite and gaspéite exhibit similar structures, consisting of rigid [CO_3] carbonate units whose oxygen atoms are corner-linked to slightly distorted metal-centered octahedra.[24–26] Due to the similar cation sizes of Mg^{2+} (0.66 Å) and Ni^{2+} (0.69 Å),[27] it is possible to form solid solutions, such as magnesian gaspéites or nickeloan magnesites, with the general formula $Ni_xMg_{1-x}CO_3$. These solid solutions have been observed in nature.[26,28] Several studies discussed the phase stability and lattice compressibility of Mg–Ni carbonate systems under high pressure (up to 50 GPa) to understand and model the deep Earth carbon cycle.[29,30] However, the carbonation behavior of Mg and Ni under CO_2 mineralization conditions ($T < 200$ °C and $pCO_2 < 200$ bar) relevant to CO_2 storage or enhanced CO_2 mineralization remains unclear. It is unknown whether they can form solid solutions or precipitate separately under these conditions. Therefore, understanding the mechanisms and compositions of Mg and Ni carbonate crystallization under moderately high temperature and high pressure conditions is crucial.

The separation of recovered Ni-carbonate from Mg-carbonate after CO_2 mineralization is important for assessing the process's feasibility and energy cost-effectiveness. Various techniques can be used to recover Ni from Ni–Mg coprecipitate carbonates; however, each has its own set of limitations. For instance, dissolving Ni–Mg coprecipitate carbonates under low pH conditions might help separate Ni-carbonate from Mg-carbonate due to their different solubilities. However, this approach may cause both carbonates to dissolve, leading to the release of CO_2 back into the atmosphere. Another method is converting Ni-carbonate to Ni-sulfide to recover Ni, but this requires further treatment, such as froth flotation, to effectively separate Ni-sulfide from Mg-carbonates. Additionally, using various ligands for complexation can selectively recover Ni, but this can pose selectivity challenges and complicate the separation process. Therefore, developing a method that eliminates the need for additional Ni recovery and refinement steps would be highly advantageous. Utilizing the coprecipitate compounds with high-value products can be promising.

Ni-carbonate has diverse applications, including its use in colored glass, nickel pigments, and electroplating solutions.[31] Recent research has demonstrated that Ni-carbonate can serve as an effective electrode material, increasing its value and potential utility. In supercapacitors, nickel-based carbonate hydroxide is employed as an electrode, demonstrating high effectiveness in reducing polarization during charging and discharging, higher reversible capacity, better structural stability, and improved electronic conductivity.[32] These properties have been attributed to its multiple oxidation states and rich redox reactions. Moreover, gaspéite has been utilized as an

electrode material for lithium battery applications.[33] Its unique lithium storage mechanism and the subsequent reversible conversion of intermediates result in an exceptionally high practical capacity. Given the excellent electrochemical properties of Ni-carbonate for electrodes in supercapacitors or lithium batteries, directly using the Mg–Ni carbonate coprecipitate offers exciting opportunities. This approach bypasses the need to convert Ni-carbonate into other Ni compounds, thus avoiding additional recovery and purification steps. Therefore, it is pivotal to investigate whether Ni-carbonate mixed with Mg-carbonate recovered from the CO_2 mineralization process can also function effectively as an electrode.

To address the aforementioned knowledge gaps, we applied a moderately high-temperature (180 °C) and high-pressure (pCO_2 = 100 bar) setup to simulate the formation of Mg and Ni carbonates after extraction from mafic/ultramafic rocks at varying Mg to Ni ratios. The compositions and morphologies of the products were analyzed using X-ray diffraction (XRD), thermogravimetric analysis (TGA), and scanning electron microscopy (SEM). Additionally, we investigated the interfacial energies obtained from density functional theory (DFT) calculations. Furthermore, we utilized the Mg and Ni carbonate products as electrodes to test their electrochemical properties and explore the possibility of directly utilizing recovered Ni-carbonates. This study enhances our understanding of CO_2 mineralization processes for the simultaneous capture of CO_2 and recovery of critical elements and provides thermodynamic calculations of the coprecipitate mineral formation. Additionally, we propose a novel application for Ni–Mg carbonate recovered from low-grade Ni and Mg resources. These materials can be used as effective electrodes for energy storage solutions, such as supercapacitors and lithium-ion batteries. Hence, this research highlights the multifaceted benefits of sustainable carbon management, resource recovery, and the development of advanced energy materials, fostering the development of more efficient and environmentally friendly energy systems.

2. Results and discussion

2.1 Core–shell structure of Mg and Ni carbonate coprecipitates

Understanding the Mg and Ni coprecipitate compositions and morphologies after the CO_2 mineralization process can provide detailed insights into the coprecipitation process of carbonates and offer guidance on the potential separation or application of Ni-carbonate and Mg-carbonate. XRD identified the composition of the Mg and Ni coprecipitate. As illustrated in Fig. 1A, magnesite and gaspéite formed after 15 hours at 180 °C and 100 bar of CO_2 pressure. Gaspéite and magnesite precipitated separately, with no formation of a Mg and Ni carbonate solid solution, as there were no observable peak shifts. Furthermore, with increasing Ni concentration, the intensity of the gaspéite peak, characterized by the peak at 32.56° (1 0 4), increased. Specifically, as shown in Fig. 1B, the weight percentage of the crystalline gaspéite fraction (obtained using the Rietveld refinement analytical method) increased from 23.4% to 40.2%, and further to 48.8% as the Ni concentration increased from 5 mM to 10 mM, and then to 20 mM. Additionally, inductively coupled plasma optical emission spectrometry (ICP-OES) (Fig. 1C) results indicated that over 98.0% of Mg and Ni were precipitated after the reactions.

TGA was used to investigate the mixtures' thermal decomposition temperatures and weight percentage (Fig. 1D). Unlike XRD, which only accounts for the crystalline phases in its composition analysis in this study, TGA can detect both amorphous and crystalline phases. By comparing the results from these two methods, we can determine if an amorphous phase was present in the system. Fig. S1 shows that pure magnesite decomposed at 519 °C, while pure gaspéite decomposed at 456 °C. The lower decomposition temperature of gaspéite compared to magnesite was consistent with the decomposition energies calculated with DFT in this study: 81.7 kJ mol^{-1} and 113.3 kJ mol^{-1} for gaspéite and magnesite, respectively. The lower decomposition energy of gaspéite indicated that less energy was required to break its bonds, resulting in a lower decomposition temperature.[34] Additionally, as the Ni concentration increased, the decomposition temperature decreased due to the higher percentage of gaspéite. Overall, the proportions of magnesite and gaspéite in the precipitates were consistent across theoretical calculations and TGA and XRD analyses, as shown in Table S1. Additionally, the TGA results aligned with the XRD results, confirming no amorphous particles formed.

From the SEM-backscattered electrons (SEM-BSE) images in Fig. 2A-a–D-a (first row), we observed that all the particles exhibited a rhombohedral morphology, as expected based on the crystal structure of magnesite and gaspéite. Magnesite and gaspéite belong to the trigonal crystal system with *R*3*c* symmetry and feature a rhombohedral primitive unit cell.[35] This structure consists of alternating sheets of cations (such as Mg^{2+} or Ni^{2+}) and CO_3^{2-} anions arranged in a hexagonal pattern. However, magnesite and gaspéite particles could not be distinguished because of their structural similarities. Cross-sections of the samples (Fig. 2A-b–D-b, second row) revealed a core–shell structure. The lighter color indicates an area with heavier elements (higher atomic number), while a darker color represents an area with lighter elements (lower atomic number). When referring to the Ni–Mg carbonate system in this paper, the outer layer contained Ni, while the inner region consisted of Mg. It is also confirmed by the Ni elemental maps obtained through energy-dispersive X-ray spectrometry (EDX), as shown in Fig. 2A-c–D-c (third row) for various Mg/Ni ratios. Additional elemental mapping results for Mg and O are presented in Fig. S2. Combining these findings with the previous XRD results, we concluded that the outer and inner layers consisted of gaspéite and magnesite, respectively.

To further investigate the interface structure between gaspéite and magnesite at the nanoscale, we prepared a core–shell structure of the Mg : Ni 20 : 20 sample. This investigation provides insights into lattice mismatch and composite configuration. The sample was thinned to approximately 10 nm using a

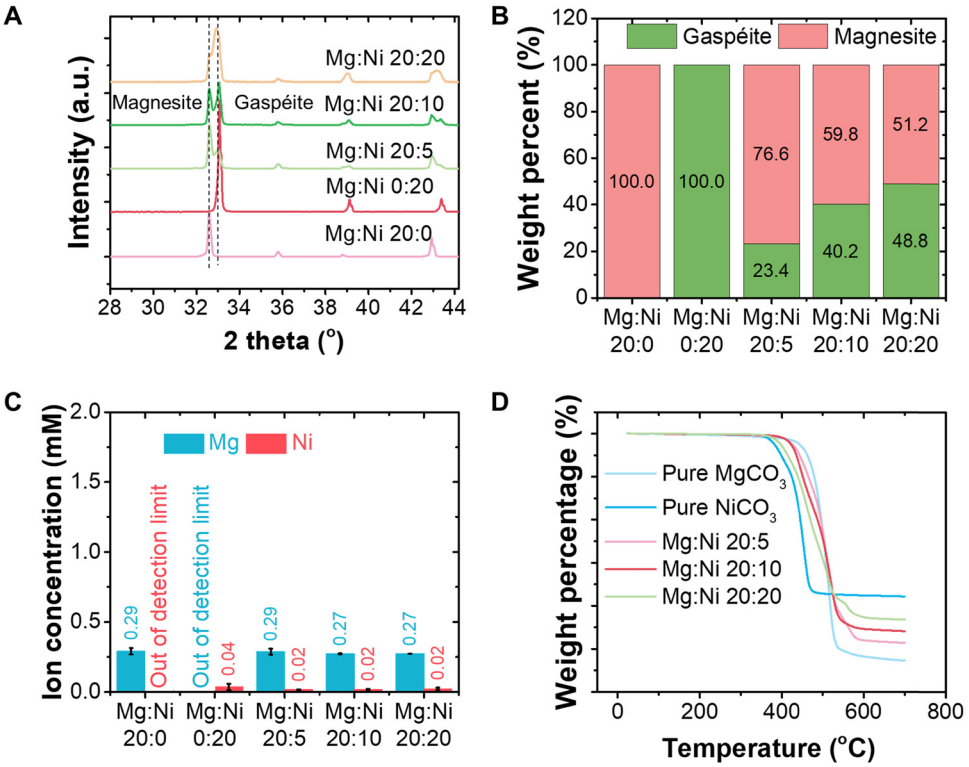

Fig. 1 Compositions of Ni and Mg carbonate precipitates. (A) The XRD analysis indicates the formation of magnesite and gaspéite, rather than a solid solution. (B) The XRD Rietveld refinement results show an increase in the weight percentage of gaspéite as the Ni concentration increases. (C) Mg and Ni aqueous concentrations after reactions at T = 180 °C and pCO_2 = 100 bar, with a measurement error of 0.02 mM for Ni, indicating that Ni and Mg were almost completely consumed. (D) The TGA results demonstrate that, as the Ni content increases, the decomposition temperature shifts to lower temperatures.

focused ion beam (FIB) and then examined at high resolution using transmission electron microscopy (TEM). The TEM images in Fig. 2E show a clear core–shell structure, with the outer layer composed of Ni and the inner region of Mg (Fig. 2F–H), consistent with the SEM images. The high-resolution TEM image of a particle corner (the yellow circle in Fig. 2E) shows the lattice differences between the particle core and shell (Fig. 2I). As shown in Fig. 2I, an interface can be observed where the magnesite side appears diffused, while the gaspéite side is more distinct. This difference can result from the high beam-sensitivity of magnesite compared to gaspéite. However, it was difficult to observe any differences in d-spacing between gaspéite and magnesite due to the relatively small differences between these crystal structures. Specifically, the theoretical d-spacing values for the (104) plane for magnesite and gaspéite were 3.88 Å and 3.85 Å, respectively. Additionally, the lattice mismatch between magnesite and gaspéite was −2.01%, which was small and allowed for heteroepitaxial growth. This small difference was also challenging to observe in Fig. 2J. The electron diffraction (ED) pattern in Fig. 2J indicates that the sample was a single crystal, as evidenced by sharp and well-defined spots arranged in a regular array. Again, due to the slight difference in lattice structures between magnesite and gaspéite, only one set of spots was observed, and no additional companion spots were seen.

Overall, based on the above characterization, we can draw two conclusions regarding the Mg–Ni carbonates compositions and morphologies: first, magnesite and gaspéite form individually without creating a solid solution within our experiment conditions (where the Mg concentration remains at 20 mM and the Ni concentration varies from 5 mM, 10 mM to 20 mM), despite their similar crystal structures. Second, core–shell structures were formed, with magnesite as the core and gaspéite as the shell.

2.2 Magnesite serves as a substrate for gaspéite nucleation/growth

Understanding the mechanism of controlling the core–shell composite structure is important for precisely tailoring the material properties and gaining fundamental insights into mineral formation. We hypothesized that the observed core–shell particle structure resulted from the faster formation kinetics of magnesite relative to gaspéite, so magnesite served as a substrate promoting gaspéite formation. To test the carbonate formation kinetics between magnesite and gaspéite, we first decreased the reaction time to slow the kinetics. We decreased the reaction time to 1 hour at T = 180 °C and pCO_2 = 100 bar. Fig. 3A shows a prominent peak for nickel bicarbonate (or nickel hydrogen carbonate) at 14.92° and characteristic peaks for both magnesite (32.59°) and gaspéite (32.95°) after

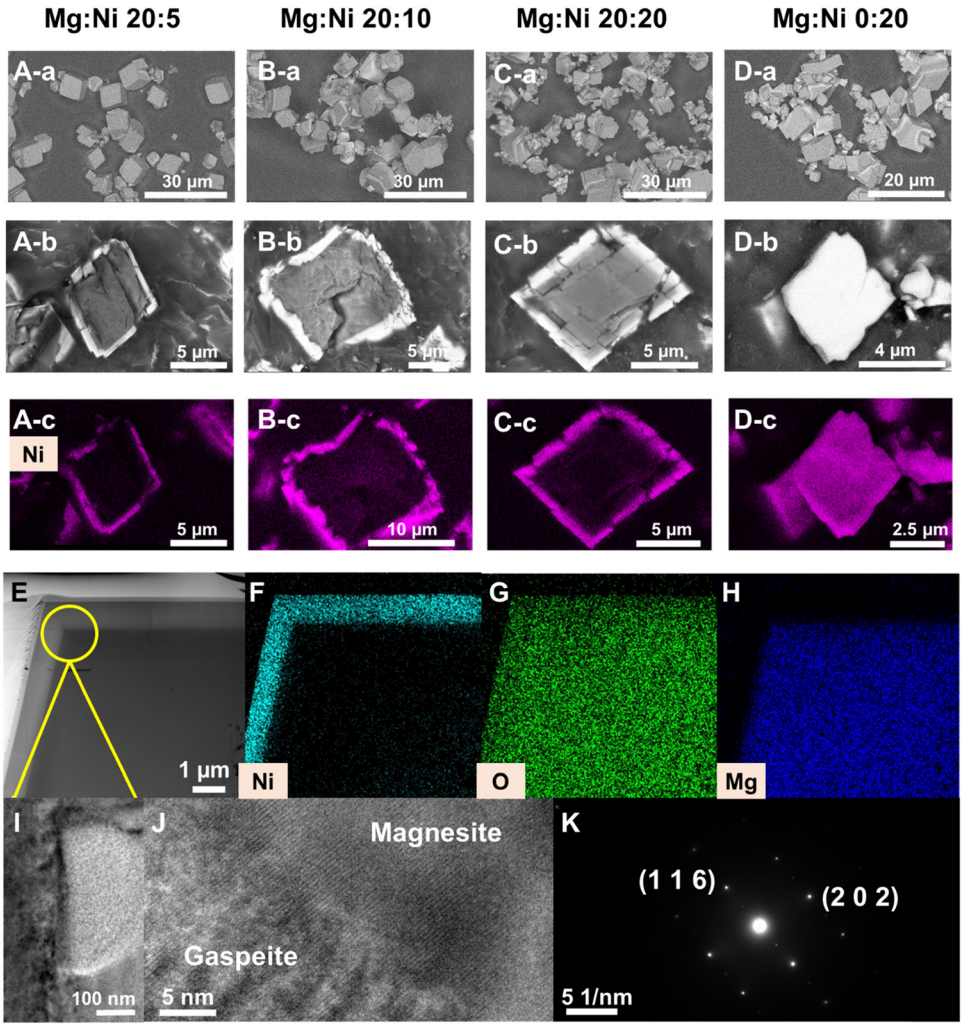

Fig. 2 Morphologies of Ni and Mg carbonate precipitates. (A-a), (B-a), (C-a), and (D-a): The SEM-BSE images reveal that rhombohedral particles were formed across all concentrations. (A-b), (B-b), (C-b), and (D-b): The cross-sections of the rhombohedral particles indicate a core–shell structure in the Mg and Ni mixture compared to pure gaspéite. (A-c), (B-c), (C-c), and (D-c): SEM-BSE images of Ni mapping shows that Ni was present in the shell. Combined with XRD results, this finding indicates that gaspéite covered the magnesite surface. Morphology and crystallinity of Ni and Mg carbonate precipitates (using Mg : Ni 20 : 20 as an example). (E) The FIB-TEM cross-sectional image shows a distinct core–shell structure. (F)–(H): Elemental mapping of Ni, O, and Mg indicates that the shell contained Ni, while the core contained Mg. (I) The zoomed-in TEM image displays a beam ring, indicating the beam was focused on the core–shell interface. (J) The HR-TEM micrograph reveals the lattice structures of magnesite and gaspéite. (K) ED pattern indicates that the particle was a single crystal.

1 hour. As the reaction time increased to 15 hours, the peak from nickel bicarbonate disappeared, and the relative intensity of the gaspéite peak at 32.95° increased compared to that of the magnesite peak at 32.59°. This peak shift indicated that nickel bicarbonate underwent phase transformation to gaspéite as the reaction time increased. It also suggested that magnesite formed initially, demonstrating faster formation kinetics. SEM images in Fig. 3B show that, in addition to the rhombohedral structures approximately 30 μm in size, there were numerous round particles around 2 μm in size (as shown in the zoomed-in image). From the results in Fig. 2, the rhombohedral particles were identified as consisting of a core–shell structure of gaspéite and magnesite, while the round particles were nickel hydrogencarbonate as indicated by XRD in Fig. 3A. As the reaction time increased to 15 hours (Fig. 3C), these small round particles disappeared, leaving only the rhombohedral particles.

Moreover, to test the carbonate formation kinetics between magnesite and gaspéite, we reduced the temperature to 130 °C while maintaining the same CO_2 pressure to slow down the reaction further. Fig. 3D shows that at 130 °C and 1 hour, the particles were a mixture of magnesite and nickel bicarbonate, with no gaspéite present. The nickel hydrogencarbonate appeared as round particles, as depicted in Fig. 3E. When the reaction time was increased to 15 hours at 130 °C, a gaspéite peak emerged alongside the magnesite peak, although a small amount of nickel bicarbonate remained. The SEM image in Fig. 3E reveals a decrease in the number of round particles and an increase in rhombohedral particles. Overall, the results lead to two conclusions: first, as the reaction time and temperature

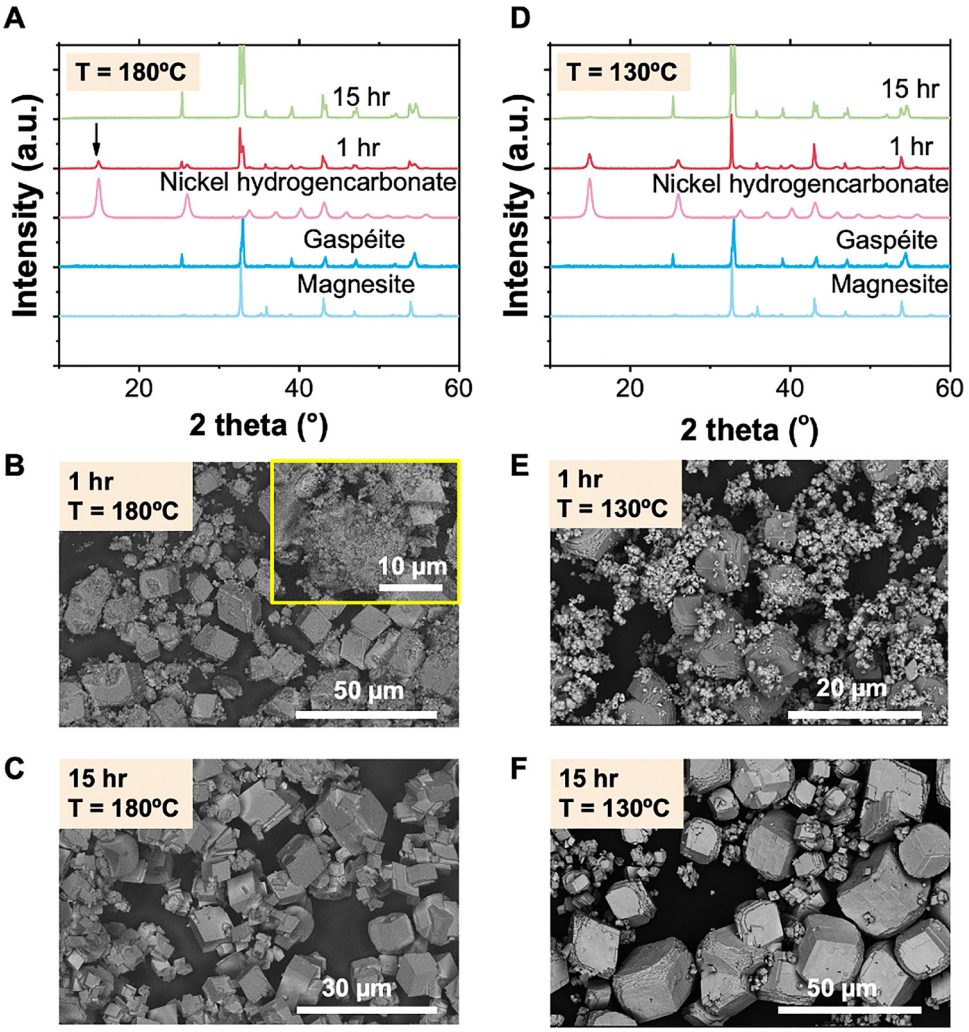

Fig. 3 Effects of temperature and reaction time on Ni and Mg carbonate precipitates. (A) XRD analysis at T = 180 °C shows that reducing the reaction time results in the formation of nickel hydrogen carbonate (known as nickel bicarbonate). (B) SEM images at T = 180 °C and t = 1 h reveals a mixture of rhombohedral and round particles. The inset shows the zoomed in image of the round particles. (C) Increasing the reaction time to 15 hours reduced the quantity of round particles. (D) XRD analysis indicates that, at T = 130 °C, more nickel hydrogen carbonate formed than at T = 180 °C for the same reaction time. (E) SEM images at T = 130 °C and t = 1 h shows numerous round particles attached to the surface of rhombohedral particles. (F) SEM images demonstrates that the number of round particles decreases as the reaction time increases, but some remain present.

increased, nickel bicarbonate converted to gaspéite. Second, magnesite forms faster than gaspéite and can serve as a substrate for gaspéite formation.

To further investigate the role of magnesite as the substrate, we conducted a two-step experiment: first, we formed magnesite separately and then observed whether gaspéite could form on its surface. By doing so, if the same core–shell structure of magnesite and gaspéite was formed, it indicated that magnesite formed faster and acted as a substrate to promote gaspéite precipitation. If not, it suggested that the other factors might control the core–shell structure formation. Specifically, first, we formed pure magnesite by mixing $Mg(NO_3)_2$ and $NaHCO_3$. Then, we added $Ni(NO_3)_2$ to form gaspéite. The SEM-BSE images in Fig. 4A and B show that the core–shell structure still formed. The mapping results in Fig. 4C indicate that the inner region contained Mg, while the outer layer contained Ni, demonstrating that the newly formed gaspéite covered the magnesite surface. These SEM results were consistent with the one-step method results shown in Fig. 2. However, we cannot exclude additional factors that may give rise to the core–shell particle structure in these experiments. For example, the core–shell structure may arise from the preferential attachment of Ni ions on the magnesite surface.

To exclude these other possibilities, we reversed the gaspéite and magnesite formation sequence using a similar two-step experiment by mixing $Ni(NO_3)_2$ and $NaHCO_3$ first and then adding $Mg(NO_3)_2$. If this reaction sequence leads to particles with gaspéite as the inner region and magnesite as the outer layer, it would indicate that the core–shell structure is due to the difference between the kinetics of the formation of magnesite and gaspéite. However, if the particles do not have a core–shell structure, it would suggest that other factors also

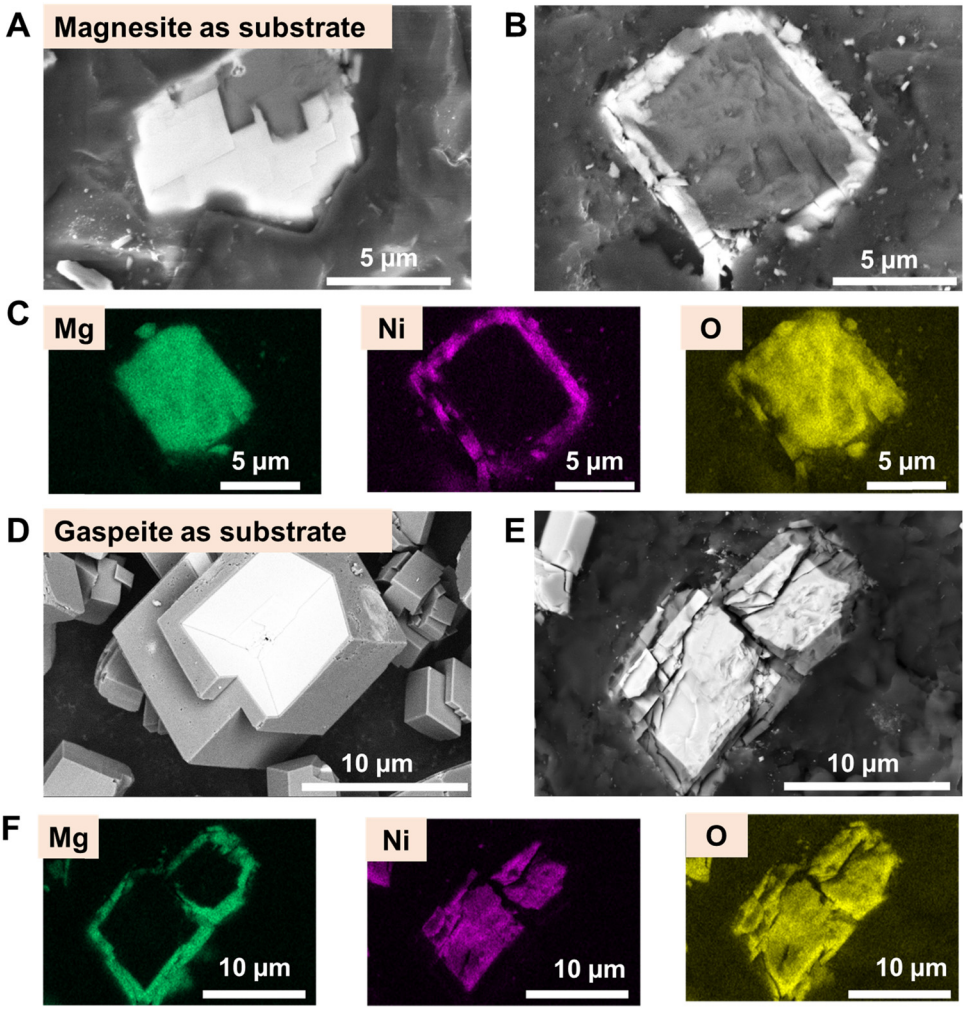

Fig. 4 The core–shell structure of carbonate particles is formed in two-step reactions. (A) SEM image shows that using magnesite as a substrate results in gaspéite formation on its surface. (B) SEM analysis indicates that the two-step method produces a core–shell structure similar to that of Mg and Ni carbonate coprecipitates. (C) Elemental mapping confirms that the shell contains Ni while the core contains Mg. (D) SEM image demonstrates the two-step method using gaspéite as the substrate. (E) SEM analysis shows the formation of a core–shell structure with the positions of magnesite and gaspéite reversed. (F) Elemental mapping confirms that, in this configuration, the shell contains Mg while the core contains Ni.

contribute to the core–shell structure formation, not just the relative kinetic differences. SEM images in Fig. 4D and E indicate that the carbonate particles adopted a core–shell structure with gaspéite as the substrate, as confirmed by mapping in Fig. 4F. XRD patterns in Fig. S3 show that for both substrates, the final compositions of the solids were the same, containing both magnesite and gaspéite, which was consistent with the results of the one-step method. The above characterization confirmed that the core–shell structure of Mg–Ni carbonate was formed because magnesite served as the substrate that subsequently promoted gaspéite formation on its surface.

From the above observations, we propose the following pathways: within a short reaction time (t = 1 hour), magnesite formed in the solution with a rhombohedral structure. Simultaneously, nickel bicarbonate formed alongside magnesite. As the reaction progressed, nickel bicarbonate underwent a phase transformation to form gaspéite, which then covered the magnesite surface, forming particles with a core–shell structure. Based on this process, we could draw the following conclusions: the kinetics of magnesite formation was faster than that of gaspéite, allowing magnesite to serve as a substrate for gaspéite growth. Additionally, no metastable phase was observed for magnesite under our experimental conditions. This could be because magnesite formed directly under high-temperature and high-CO_2 pressure conditions. It was also possible that the phase transformation occurred too fast to be observed under such conditions.

2.3 Interfacial energy profiles

Providing thermodynamic information is crucial for understanding carbonate formation and explaining the development of core–shell structures. The interfacial energy was employed to better understand the core–shell structure of magnesite and gaspéite rather than to separate particles. To quantify interfacial energies, DFT calculations were utilized. Fig. 5A shows

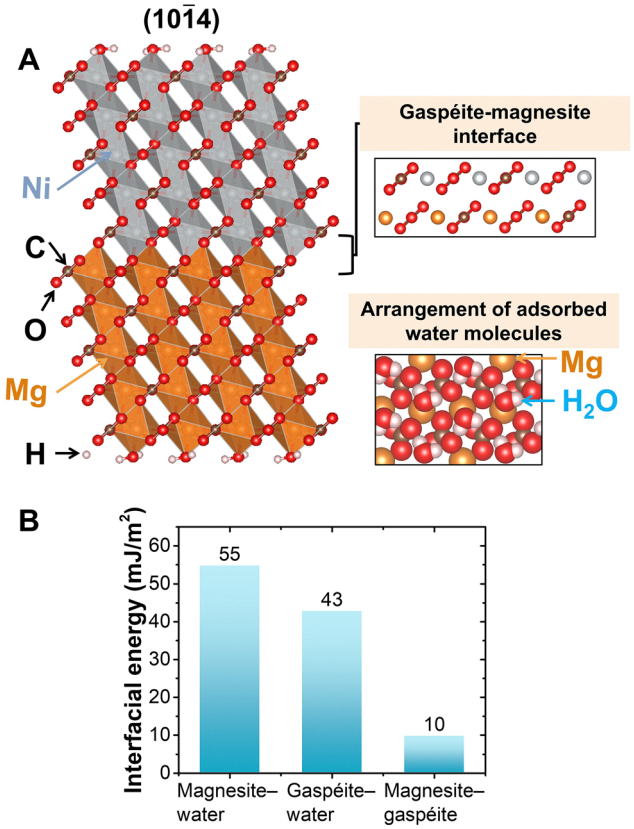

Fig. 5 Heterogeneous nucleation of gaspéite on the magnesite (10$\bar{1}$4) surface. Ball-and-stick models of the energy-minimized magnesite-gaspéite interfacial slab (A). Ni, Mg, C, O, and H atoms are shown in gray, orange, brown, red, and white balls, respectively. The insets show zoomed-in models of the interface (top, ball-and-stick model) and the arrangement of adsorbed water molecules from the top view (bottom, space-filling model). (B) Interfacial energies for three interfaces.

the energy-minimized magnesite–gaspéite slabs of (10$\bar{1}$4) surface. The structure of gaspéite and magnesite was illustrated using a ball-and-stick model, with the octahedral planes depicted in gray for gaspéite and brown for magnesite. The zoomed-in image on the top right highlighted the organization of Ni, Mg, and carbonate ions at the interface, revealing a slight lattice mismatch between the two minerals (−2.01%). The arrangement of adsorbed water molecules on the magnesite surface was displayed in the bottom image using a space-filling model. Three interfacial energies were simulated: a magnesite–water interfacial energy of 55 mJ m^{-2}, a gaspéite–water interfacial energy of 43 mJ m^{-2}, and a magnesite–gaspéite interfacial energy of 10 mJ m^{-2}, respectively, as shown in Fig. 5B.

From the above DFT results, we can draw the following conclusions: First, the gaspéite–water interfacial energy is higher than the magnesite–gaspéite interfacial energy. This indicates that the presence of magnesite as a substrate is more favorable for gaspéite formation than its absence. In other words, the heterogeneous nucleation of gaspéite on magnesite is more favorable than the homogeneous nucleation of gaspéite. This finding suggests that using magnesite as a substrate can enhance gaspéite formation. Second, the magnesite–water interfacial energy is larger than the magnesite–gaspéite interfacial energy. This implies that the higher interfacial energy of the magnesite–water interface tends to be minimized by nucleating gaspéite on the magnesite surface. This reduction in interfacial energy facilitates the formation of gaspéite. Third, the relatively small magnesite–gaspéite interfacial energy is caused by the minor lattice mismatch.

2.4 $MgCO_3$@$NiCO_3$ electrochemical properties

Pure Ni-carbonate is a promising electrode material for supercapacitors and lithium-ion batteries due to its excellent cycling stability.[32,33] However, it remained unclear whether $MgCO_3$@$NiCO_3$ compounds that we obtained from resource recovery can also be effectively used as electrode materials. Fortunately, Ni-based materials, such as nickel oxides and hydroxides, and core–shell structure particles have been widely studied as active electrodes for supercapacitors due to their rich redox activity and high theoretical capacitance. These studies highlight the broader potential of Ni-based materials—including nickel carbonates—as promising candidates for electrochemical energy-storage applications. For example, $MgCo_2O_4$@CoFe–layered double hydroxide (LDH) core–shell nanoarrays have been reported to achieve enhanced rate capability and cycling stability through a heterostructured LDH architecture.[36] Similarly, NiCoMn–LDH grown on an eggshell-like porous carbon framework demonstrates high energy density and mechanical flexibility for advanced asymmetric supercapacitor (ASC) devices.[37] In addition, $Ni(OH)_2$@$Cu(OH)_2$ core–shell nanorod arrays have shown improved charge transport and specific capacitance through hierarchical structural design.[38] These studies highlight current efforts to enhance electrochemical performance through the rational design of Ni-based composite architectures, offering useful suggestions for the development of waste-derived carbonate electrodes.

The electrochemical properties of pure gaspéite ($NiCO_3$) and Mg : Ni = 20 : 20 (referred to as $MgCO_3$@$NiCO_3$ in the following discussion) samples as electrodes in an aqueous electrolyte were tested using cyclic voltammetry (CV) and electrochemical impedance spectroscopy(EIS) in a three-electrode system with Ag/AgCl as the reference electrode and a platinum mesh as the counter electrode in 2 M KOH. The CV curves for $NiCO_3$ indicated typical faradaic capacitor behaviors (the CV of control carbonate paper is shown in Fig. S4A). Fig. S4B shows the CV results for $NiCO_3$ at scan rates ranging from 20 mV s^{-1} to 300 mV s^{-1} in the potential window of 0 to 0.52 V. The redox peaks for $NiCO_3$ were observed at 0.38 V as anodic peaks and 0.31 V as cathodic peaks, corresponding to eqn (1) (as shown in Fig. 6A). Due to the polarization of the electrode, the anodic peak gradually shifted to a higher potential, and the cathodic peak shifted to a lower potential with the increasing scan rate, respectively. However, the general shape of the CV curves does not change greatly with the scan rate, which implies that the electrode materials possess a high-rate capability.

$$NiCO_3 + 3OH^- \rightleftharpoons NiOOH + CO_3^{2-} + H_2O + e^- \quad (1)$$

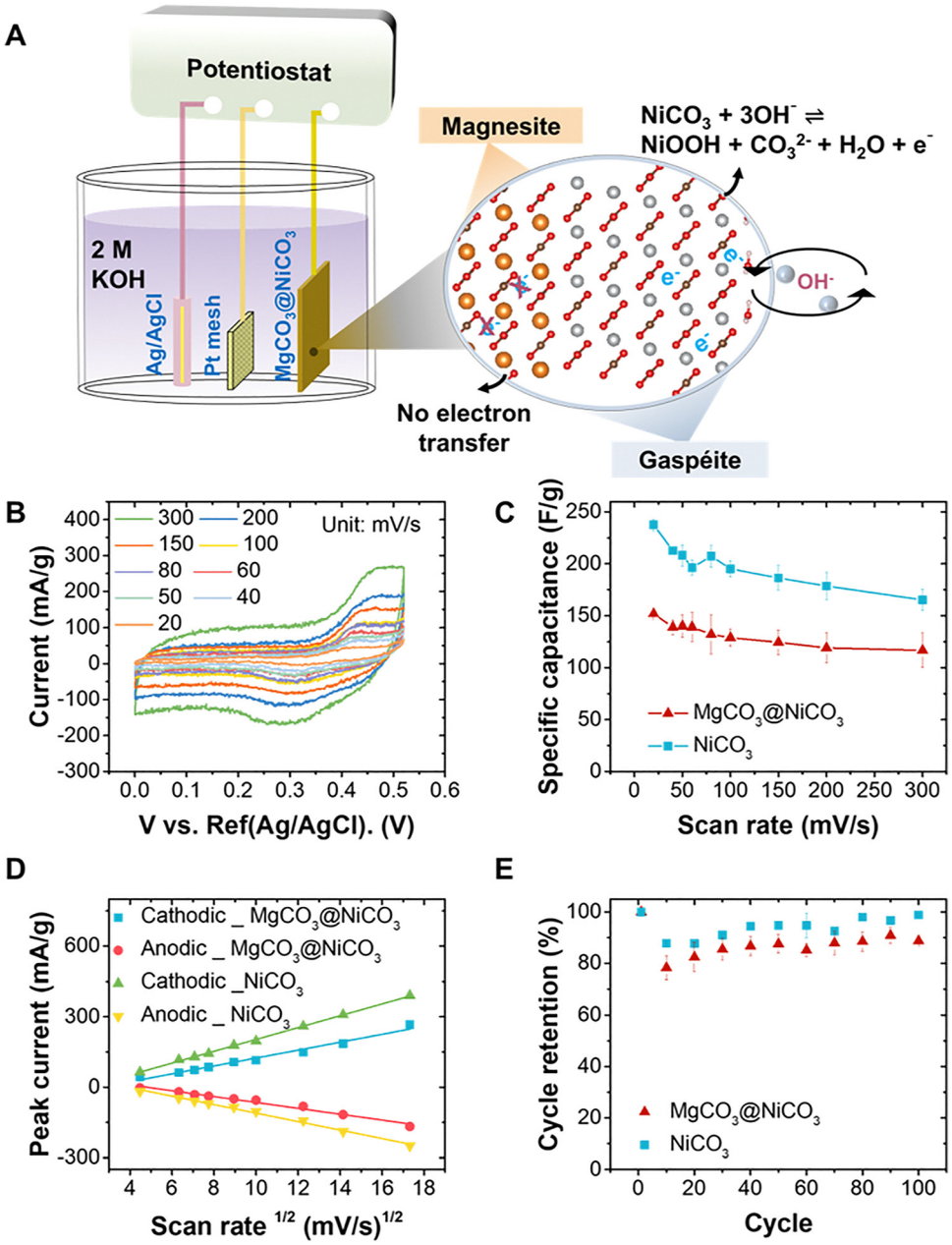

Fig. 6 Electrochemical properties of $MgCO_3$@$NiCO_3$ materials. (A) A schematic diagram of the electrochemical testing. The electrolyte used was 2 M KOH, and only the shell of gaspéite was reactive. (B) CV curves for the recovered $MgCO_3$@$NiCO_3$ materials as electrodes, with scan rates ranging from 20 mV s^{-1} to 300 mV s^{-1}. (C) Specific capacitance was calculated from the CV curves for both gaspéite and $MgCO_3$@$NiCO_3$. (D) Ion diffusion rate calculated from anodic and cathodic peaks of CV curves. (E) Cycling stability was tested after 100 cycles of CV measurement at 50 mV s^{-1}, and the error bars were smaller than the symbols. All experiments were conducted in triplicate.

As the scan rate decreased in Fig. S4B, a new cathodic peak appeared at 0.25 V, while no additional anodic peaks were observed. The possible explanation for the emergence of the new cathodic peak at lower scan rates is a secondary reduction process or the formation of an intermediate species that becomes more pronounced at slower scan rates. This secondary process may not have a corresponding anodic peak due to the reduced species' irreversibility or stability under the given experimental conditions.[39] Fig. 6B shows the CV curves for the $MgCO_3$@$NiCO_3$ electrode tested under the same conditions. The redox peaks for $MgCO_3$@$NiCO_3$ were observed at 0.43 V as anodic peaks and 0.31 V as cathodic peaks, corresponding to the $NiCO_3$ redox reaction. The anodic peak for $MgCO_3$@$NiCO_3$ shifts to a higher voltage than pure $NiCO_3$, which can be caused by the presence of $MgCO_3$. Incorporating $MgCO_3$ may alter the electronic environment and increase the overpotential required for the oxidation process, leading to a shift in the anodic peak.[39]

Fig. 6C shows the specific capacitance calculated and normalized by the electrode weight at different scan rates for

$NiCO_3$ and $MgCO_3$@$NiCO_3$ electrodes, where both electrodes had the same initial Ni precursor concentrations as 20 mM. The specific capacitances for both electrodes decrease as the scan rate increases due to the limited time for ion diffusion into the electrode pores at higher scan rates. $NiCO_3$ has a higher capacitance than $MgCO_3$@$NiCO_3$. For instance, at a scan rate of 50 mV s^{-1}, the capacitances were 218.47 F g^{-1} for $NiCO_3$ and 151.01 F g^{-1} for $MgCO_3$@ $NiCO_3$. The relatively lower capacitance for $MgCO_3$@$NiCO_3$ is attributed to the lower weight percentage of the active material $NiCO_3$ in $MgCO_3$@$NiCO_3$ compared to pure $NiCO_3$. This normalization provides a realistic assessment of the performance of the as-recovered material rather than an artificially enhanced value based solely on the active $NiCO_3$ fraction. Importantly, because the carbonates were directly recovered from waste-derived feedstock, the results also demonstrate new potential of integrating sustainable resource recovery with electrochemical energy-storage applications, highlighting a path toward low-cost and environmentally responsible electrode materials.

Fig. 6D illustrates the relationship between the oxidation peak current and the reduction peak current with the square root of the scan rate ($\nu^{1/2}$) for $NiCO_3$ and $MgCO_3$@$NiCO_3$. The good linear correlations indicated that the electrochemical process is mainly diffusion-controlled. $NiCO_3$ exhibits a higher slope than $MgCO_3$@$NiCO_3$, indicating that $NiCO_3$ has faster electron transfer kinetics. Additionally, galvanostatic charge–discharge (GCD) measurements at 0.5, 1, 2 mA cm^{-2} (Fig. S5A) were used to evaluate the electrochemical response of the $MgCO_3$@$NiCO_3$ electrode. The GCD profiles show a noticeable asymmetry, where the charging time is longer than the discharge time, suggesting that the charge-storage process involves slower ion transport or a kinetically limited redox step. As shown in Fig. S5B, the cycling performance obtained from CV measurements at 50 mV s^{-1} displays a mild but consistent activation behavior, in which the specific capacitance gradually increases and then remains stable over 1000 cycles. This trend indicates that repeated cycling may slightly improve electrolyte accessibility. Also, it is likely due to the gradual activation of $NiCO_3$ into electrochemically active $Ni(OH)_2$.

The EIS analytical method was applied to further investigate the ion transport properties and system impedance of the $MgCO_3$@$NiCO_3$ composites from the coprecipitation of mixed solutions. Fig. S5C shows the Nyquist plots for the $NiCO_3$ and $MgCO_3$@$NiCO_3$ electrodes (zoomed in image of the plot shown in Fig. S5D). The equivalent circulate (EC) $R_1(CR_2)(QR_3)$ was used in the simulation,[40] corresponding to the simplified physical model of an open pore structure. In the EC, R_1 is solution resistance, R_2 is pore electrolyte and intermediate layer resistance, Q is constant phase element, C is capacitance, and R_3 is resistance of the barrier layer. The simulation results are shown in Table S2. Fig. 6E presents the cycling stability of $NiCO_3$ and $MgCO_3$@$NiCO_3$ electrodes. The results showed that after 100 cycles, the $NiCO_3$ and $MgCO_3$@$NiCO_3$ electrodes retained 97.87% and 90.14% of their initial capacity, respectively. This indicated that both electrodes had good reusability. Furthermore, the data suggested that incorporating $MgCO_3$ as the core in the electrodes did not negatively affect their cycling stability. Overall, from the above electrochemical characterization, we found that the recovered $MgCO_3$@$NiCO_3$ can be applied as supercapacitor electrodes with good capacitance and cycling stability. Our results shed light on the viability of the recovered $MgCO_3$@$NiCO_3$ as an electrode. Despite being recycled, its performance closely mirrored the pure $NiCO_3$, highlighting its efficiency.

To further evaluate the practical energy storage performance of the $MgCO_3$@$NiCO_3$ electrode, an asymmetric supercapacitor (ASC) device ($MgCO_3$@$NiCO_3$//AC) was assembled using the $MgCO_3$@$NiCO_3$ composite as the positive electrode and activated carbon (AC) as the negative electrode, with 2 M KOH as the electrolyte. Fig. S6A shows the cyclic voltammetry (CV) curves of the $MgCO_3$@$NiCO_3$//AC device at a scan rate of 50 mV s^{-1}. As the potential window expanded, the CV curves retained similar shapes, indicating good reversibility and the absence of side reactions up to 1.2 V. Fig. S6B presents the GCD curves at a current density of 0.1 mA cm^{-2}, further confirming stable electrochemical behavior.

As shown in Fig. S6C, the CV curves obtained at scan rates from 10 to 300 mV s^{-1} within 0–1.2 V display an increasing area with higher scan rates while maintaining their shape, demonstrating fast ion transport and stable capacitance behavior. Fig. S6D shows the GCD profiles at different current densities, where the discharge time decreases with increasing current density, consistent with typical capacitive characteristics. The calculated specific capacitance of the $MgCO_3$@$NiCO_3$//AC ASC device is approximately 7 F cm^{-2} (Fig. S6E). As shown in Fig. S6F, the cycling performance reveals an initial increase in capacitance during the first 400 cycles, likely due to the gradual activation of $NiCO_3$ into electrochemically active $Ni(OH)_2$, followed by stable long-term cycling with high capacitance retention, indicating good durability and activation stability of the electrode material. The energy density and power density were evaluated to assess the overall energy storage performance of the asymmetric supercapacitor. The corresponding Ragone plot is shown in Fig. S7. $MgCO_3$@$NiCO_3$ has a relatively low performance, which is consistent with CV and GCD results.

To benchmark the $MgCO_3$@$NiCO_3$ recovered electrode material against a commercial Ni-based supercapacitor electrode, we tested $Ni(OH)_2$ in a three-electrode configuration. CV was conducted to quantitatively compare the electrochemical behavior of $MgCO_3$@$NiCO_3$ and $Ni(OH)_2$ electrodes. As shown in Fig. S8A, $Ni(OH)_2$ displays a significantly larger CV area across the tested potential window, reflecting its intrinsically higher pseudo-capacitance arising from rapid and reversible Ni^{2+}/Ni^{3+} redox transitions. $MgCO_3$@$NiCO_3$, in contrast, exhibits a more restricted CV envelope, consistent with its limited redox accessibility and lower charge-storage capability during the initial cycles. This difference is expected, as $Ni(OH)_2$ is a well-known benchmark pseudocapacitive material, whereas $MgCO_3$@$NiCO_3$ is electrochemically less active before any structural transformation. Also, $MgCO_3$ from $MgCO_3$@$NiCO_3$ does not contribute to the capacitance, making the absolute value of $MgCO_3$@$NiCO_3$ relatively low.

Long-term cycling stability (up to 1000 cycles) reveals a divergence between the two materials (Fig. S8B). While $Ni(OH)_2$ maintains a higher absolute capacitance throughout cycling, it undergoes the typical gradual decay associated with structural fatigue and partial loss of electrochemically active sites. $MgCO_3$@$NiCO_3$, however, exhibits an opposite trend: its capacitance steadily increases with cycle number, showing a clear activation behavior. This enhancement suggests that repeated redox cycling might be caused by a partial *in situ* conversion of $MgCO_3$@$NiCO_3$ into more electrochemically active phases (*e.g.*, hydrated $Ni(OH)_2$/NiOOH), which might be caused by improved electrode wetting,[41] or enhanced conductivity.[42] Such electrochemical conditioning transforms initially inert carbonate domains into redox-active species, enabling gradual performance enhancement rather than degradation. These contrasting trends highlight the fundamentally different charge-storage mechanisms in $MgCO_3$@$NiCO_3$ and $Ni(OH)_2$, and further demonstrate that $MgCO_3$@$NiCO_3$ may function as the ''activating'' electrode material with performance that improves under long-term operation. In addition, the $MgCO_3$@$NiCO_3$ composite offers a distinct advantage in terms of sustainability. These materials can be obtained from recovered materials sourced from low-grade ore, and can provide a resource-efficient and environmentally responsible alternative, strengthening its circular economy.

This underscored the potential of the material recovery process in creating high-performance electrodes. Additionally, using recovered materials can reduce dependency on raw materials and lower production costs. High-performance electrodes from recycled materials enhance sustainability in energy storage systems such as batteries and supercapacitors. This approach promoted a circular economy and supports energy technology innovation.

3. Conclusions

This study demonstrates the formation of a core–shell structure when Ni and Mg coprecipitate at a temperature of 180 °C and a CO_2 pressure of 100 bar. In this structure, magnesite ($MgCO_3$) precipitates as the core, while gaspéite ($NiCO_3$) forms the shell. This phenomenon was attributed to the relatively faster precipitation rate of magnesite compared to gaspéite. DFT simulations indicated that magnesite served as a substrate, lowering the interfacial energy compared to homogeneous nucleation without a substrate. Furthermore, the recovered $MgCO_3$@$NiCO_3$ core–shell structure exhibited excellent electrochemical properties, making it a promising candidate for electrode materials. The compound demonstrated high capacitance and stable cyclability. The $MgCO_3$ matrix acts as the structural core, while $NiCO_3$ forms the active electrochemical shell. With the same $NiCO_3$ content, pure $NiCO_3$ exists as a bulk phase, limiting electron transport and ion diffusion. In the $MgCO_3$@$NiCO_3$ composite, however, $NiCO_3$ forms a thin shell that shortens diffusion paths, increases electrolyte accessibility, and provides more efficient electron-transport pathways. This architecture enables higher electrochemical utilization of $NiCO_3$. Moreover, forming composites allows direct use of mixed Mg–Ni feedstocks without energy-intensive separation or high-temperature processing, reducing waste, cost, and environmental impact while converting low-grade minerals into functional materials.

Our study has several important implications: First, the coprecipitation behavior of Ni and Mg can be applied to Ni extraction from other leachates, such as electronic waste and mining wastewater, which contain varying Ni to Mg ratios. Second, the research provides a method for CO_2 capture and mineralization by forming Mg and Ni carbonates, enhancing CO_2 capture capacity compared to traditional Ni extraction methods. Third, directly using the recovered carbonate materials as electrode candidates simplifies the process, avoiding the need for further additional processing of $NiCO_3$ into other forms, such as sulfide compounds. This reduction in processing steps can decrease the overall cost of electrode synthesis. Lastly, the recovered material from the CO_2 mineralization process can be directly used as electrodes, contributing to energy storage in several significant ways. By repurposing this material, we can reduce the dependence on newly extracted raw materials, leading to cost savings and resource efficiency. This research offers a novel approach to Ni recovery and utilization, contributing to more efficient resource use and environmental sustainability. This highlights that recycled materials can reduce raw material dependency and production costs. This promotes sustainability in energy storage systems such as batteries and supercapacitors. The approach supports a circular economy and advances green energy technologies.

4. Materials and methods

4.1 Materials

All aqueous solutions used in this study were prepared using deionized water (DI) with a minimum conductivity of $\geq$18.2 MΩ cm (Milli-Q, IQ 7000, Sigma Millipore). Chemical reagents employed had a grade meeting at least the American Chemical Society (ACS) standard. Sodium bicarbonate ($NaHCO_3$) was purchased from VWR International, PA. Magnesium nitrate ($Mg(NO_3)_2{\cdot}6H_2O$), carbon black, polyvinylidene fluoride (PVDF, average MW 534 000), potassium hydroxide (KOH), and *N*-methyl-2-pyrrolidone (NMP) were purchased from Sigma-Aldrich, MO. Araldite 502 embedding kit, nickel nitrate ($Ni(NO_3)_2{\cdot}6H_2O$) was purchased from Ward's Science, NY.

4.2 Coprecipitation of magnesium carbonate and nickel carbonate

To simulate the CO_2 mineralization conditions for mafic/ultramafic rocks and other waste streams, a high-temperature and high-pressure setup was employed in the experiments, as shown in Fig. S9. The carbonation experiments were performed at a temperature of 180 °C and a CO_2 pressure of 100 bar for 15 hours. These conditions fall within the supercritical CO_2

($ScCO_2$) regime ($T > 31.1$ °C and $P > 73.8$ bar). $ScCO_2$ was used to simulate conditions relevant to geologic CO_2 storage (*in situ* carbonation) and to provide insights into increasing reactivity for *ex situ* carbonation conditions.[43] In the first series of experiments, Mg and Ni nitrate solutions were prepared with the following Mg and Ni concentrations, respectively: 20 mM : 0 mM, 20 mM : 5 mM, 20 mM : 10 mM, and 20 mM : 20 mM and then reacted with 0.5 M $NaHCO_3$. The Ni concentration fell within the range observed for both mafic rock dissolution, electronic waste[12] and laterite waste[44] Ni concentrations. The saturation indexes of the aqueous phase relative to magnesite and gaspéite, defined as $\ln(Q/K_{sp})$ – where Q is the ion activity product and K_{sp} is the solubility product constant, were calculated and reported in Table S3.

To investigate the mechanisms of carbonate formation and the kinetics of magnesite and gaspéite formation, a second series of experiments were performed by adding Mg and Ni sequentially. First, we prepared a 100 mL solution of 20 mM $Mg(NO_3)_2$ and 0.5 M $NaHCO_3$ and let the solution react at 180 °C and pCO_2 = 100 bar for 15 hours. In the second step, we added $Ni(NO_3)_2$ salt to the above samples to achieve a Ni concentration of 20 mM and let the solution react for another 15 hours. Second, the same procedure was followed to determine if gaspéite can serve as a substrate for magnesite growth. Specifically, we prepared a 100 mL solution containing 20 mM $Ni(NO_3)_2$ and 0.5 M $NaHCO_3$ and allowed it to react for 15 hours. In the second step, we added $Mg(NO_3)_2$ salt to the 100 mL solution to achieve a final Mg concentration of 20 mM and continued the reaction for 15 hours. After the reactions, the samples were centrifuged, and the solids were dried in an oven at 60 °C and ambient pressure for 24 hours. The dried samples were then used for further characterization.

4.3 Characterization of aqueous solutions and solids

To elucidate morphological and elemental composition changes, the samples were analyzed *via* scanning electron microscopy (SEM, JEOL 7001LVF FE-SEM) coupled with energy-dispersive X-ray spectrometry (EDX). The cross-section samples were prepared using the Araldite 502 kit with benzyldimethylamine (BDMA). Specifically, 1.25 mL of eponate 12 Resin, 0.75 mL of Araldite 502, 3 mL of dodecenyl succinic anhydride (DDSA), and 0.15 mL of BDMA were mixed at room temperature for 10 minutes. This mixture was then mixed with the powder samples and cured in an oven at 70 °C for 24 hours. After curing, the samples were polished using sandpaper of varying grit sizes. Finally, the polished samples were analyzed using SEM.

To characterize the crystalline structure of the samples, transmission electron microscopy (TEM, JEOL JEM-2100F) was employed. The TEM samples were prepared using focused ion beam-scanning electron microscopy (FIB-SEM, Thermofisher Scios 2). The TEM images were analyzed with the Image J software. Elemental mapping was performed using a Bruker Quantax 200 system with an X-flash silicon drift detector (SDD). The lattice mismatch (f) of (1 0 4) surfaces of gaspéite and magnesite was calculated using eqn (2). Furthermore, to examine the sample composition after the reactions, samples were analyzed with X-ray diffraction (XRD, Bruker d8 Advance). Additionally, thermogravimetric analysis (TGA, TA instruments Q5000) was employed to analyze the thermal stability and composition of the samples. The temperature was ramped up to 700 °C at 10 °C min^{-1} under a nitrogen (N_2) atmosphere. Eqn 3 and 4 were used to calculate the theoretical and measured weight percentages of magnesite and gaspéite. The centrifuged solution was filtered using a 0.22 μm filter, and the ion concentrations were then measured using inductively coupled plasma optical emission spectrometry (ICP-OES, PerkinElmer Optima 7300DV).

$$f = \frac{SA_2 - SA_1}{SA_1} \times 100 \quad (2)$$

where SA_1 = 33.98 Å^2 (the area of the magnesite $(10\bar{1}4)$ surface unit cell), and SA_2 = 33.30 Å^2 (the area of the gaspéite $(10\bar{1}4)$ surface unit cell), leading to $f = -2.01\%$.

$$MCO_3 \rightarrow MO + CO_2, \quad M = Mg \text{ or } Ni \quad (3)$$

$$C = \frac{MO}{MCO_3} \times 100 \quad (4)$$

$$X = \frac{0.629 - L}{0.151} \quad (5)$$

$$Y = 1 - \frac{0.629 - L}{0.151} \quad (6)$$

After the TGA decomposition process, the theoretical remaining weight percentage (C) was calculated using eqn (4). For example, the molecular weights are 40.30 g mol^{-1} for MgO and 84.31 g mol^{-1} for $MgCO_3$. Using eqn (4), we calculated a C value of 47.80% for pure magnesite. Similarly, the molecular weights of NiO and $NiCO_3$ are 74.69 g mol^{-1} and 118.70 g mol^{-1}, respectively, resulting in a C value of 62.92% for pure gaspéite.

To determine the percentages of magnesite and gaspéite in the composite, we compared the theoretical percentages with those obtained from the TGA results. For the theoretical percentages, we assumed that Mg and Ni precipitated as magnesite and gaspéite, respectively. For example, with a Mg : Ni concentration ratio 20 : 10, the reaction yields 2/3 magnesite and 1/3 gaspéite in mole fractions. Converting these mole fractions into weight percentages, we find that magnesite ($MgCO_3$) constitutes 58.69% and gaspéite ($NiCO_3$) constitutes 41.31% of the total. To calculate magnesite and gaspéite composition from TGA, eqn (5) and (6) were used to calculate the weight percentage for the synthesized samples, where X was the weight percentage for gaspéite, Y was the weight percentage for magnesite, and L was the weight loss percentage obtained from TGA. More detailed calculation processes are shown in supplementary information (SI) Note S1.

4.4 Density functional theory calculations

To explain the formation of core–shell structure particles, the interfacial energies of the interfaces must be known. We obtained these interfacial energies using DFT calculations.

DFT calculations were performed with VASP (Vienna *ab initio* simulation package)[45–48] using the projector augmented-wave (PAW) approach.[49,50] Two exchange–correlation functionals were used in the calculations: the Perdew, Burke, and Ernzerhof (PBE) approximation[51,52] augmented by the Grimme (D3) dispersion corrections[53] and the hybrid PBE0 functional.[54] The PAW potentials were obtained from the VASP database for hydrogen (0), carbon (2), oxygen (2), magnesium (4), and nickel (18) with the number of core electrons shown in parentheses. The Hubbard on-site correction (+U) was applied to the 3d orbitals of Ni using the rotationally invariant method of Dudarev.[55] The effective Hubbard correction (U_{eff} = 2 eV) determined by Sassi and Kerisit (2024)[56] based on a range of Ni-containing phases was used in this work. For all the calculations, the cutoff energy for the plane-wave basis set was fixed to 520 eV (1.3 times the highest default cutoff energy of 400 eV (for C and O) among all atoms considered), and the convergence criterion for the electronic self-consistent calculation was 10^{-5} eV. Convergence was reached in the energy minimizations when the force on any atom was less than 0.01 eV Å^{-1}. A more detailed DFT calculation description is shown in SI Note S2.

4.5 Electrode preparation and electrochemical property tests

To prepare working electrodes, the samples were mixed with carbon black and PVDF in a weight ratio of 8 : 1 : 1. This mixture was then dispersed in NMP to form a homogeneous viscous slurry. The slurry was subsequently painted onto a piece of conductive carbon paper (MSE supplies, which has a thickness of 0.3 mm and an electrical resistivity of 3 mΩ cm^{-2}), to use as the current collector. The working electrodes were dried in an oven at 60 °C for 12 hours to remove the solvent. The bare conductive carbon paper was used as the control.

The electrochemical performance was tested using a conventional three-electrode system. The as-prepared electrode was used as the working electrode, Pt was used as the counter electrode, and an Ag/AgCl electrode (Basi, 3 M KCl) was used as the reference electrode. A Gamry Potentiostat (reference 600+) was used to test the electrochemical properties in a 2 M KOH aqueous solution as the electrolyte. The cyclic voltammetry (CV) tests were carried out within a voltage range from 0 V to 0.52 V at various scan rates. Electrochemical impedance spectroscopy (EIS) measurements were performed in the 100 kHz–0.1 Hz frequency range at the open circuit potential. The specific capacitance of electrodes (C_s) is calculated using eqn (7):

$$C_s = \frac{\int_{V_i}^{V_f} i\,dV}{mv\Delta V} \tag{7}$$

where m is the mass of the active material (g), v is the scan rate (V s^{-1}), ΔV is the difference between the initial, V_i, and final, V_f, potentials (V) in the scan, and i is the current (mA).

The cycle retention (R) is calculated using eqn (8):

$$R = \frac{\text{Capacity after } N\text{th cycles}}{\text{Initial capacity}} \times 100\% \tag{8}$$

The detailed electrochemical tests, including galvanostatic charge–discharge (GCD), asymmetric supercapacitor (ASC) configuration, and electrochemical testing of a commercial $Ni(OH)_2$ electrode, are described in SI Notes S3–S5.

Conflicts of interest

There are no conflicts to declare.

Data availability

All data are available in the main text or the supplementary information (SI) and are also available from the corresponding authors on reasonable request. Supplementary information: Table S1 Comparison of magnesite and gaspéite composition using different methods; Table S2 EIS simulation results for pure $NiCO_3$ and $MgCO_3$/$NiCO_3$ electrodes; Table S3 Saturation ($\sigma = \ln Q/K_{sp}$) with respect to magnesite and gaspéite and pH values at T = 180 °C and pCO_2 = 100 bar; Note S1 Thermogravimetric analysis (TGA) weight percentage calculations; Note S2 Density functional theory calculations; Note S3 Galvanostatic charge–discharge (GCD) measurements; Note S4 Asymmetric supercapacitor (ASC) configuration and electrochemical measurements; Note S5 Electrochemical testing of commercial $Ni(OH)_2$ electrode; Fig. S1 The weight deviation observed from TGA indicates that the decomposition temperatures for magnesite and gaspéite are 519 °C and 456 °C, respectively; Fig. S2 Mapping of elements O and Mg for different Mg to Ni ratio samples; Fig. S3 The XRD was obtained through a two-step experiment where the sequence of adding $Mg(NO_3)_2$ and $Ni(NO_3)_2$ was varied; Fig. S4 CV test for carbon papers and pure gaspéite; Fig. S5 Electrochemical tests for $MgCO_3$@$NiCO_3$; Fig. S6 Electrochemical properties test of ASC in a two-electrode system; Fig. S7 Ragone plot of $MgCO_3$@$NiCO_3$//AC electrode; Fig. S8 Comparison of $MgCO_3$@$NiCO_3$ and $Ni(OH)_2$; Fig. S9 The diagram illustrates the high-temperature, high-CO_2-pressure (high T and P) reactor system used in our experiments. See DOI: https://doi.org/10.1039/d5mh01407g.

Acknowledgements

This work was supported by the U.S. Department of Energy (DOE), Office of Science, Office of Basic Energy Sciences, Chemical and Materials Sciences to Advance Clean Energy Technologies and Low-Carbon Manufacturing (DE-SC0023390 for YW and YSJ and FWP 80281 for SNK). The Chemical and Environmental Analysis Facility and the Institute of Materials Science & Engineering at Washington University in St. Louis provided their facilities for the experiments. The authors acknowledge the members of the Environmental NanoChemistry Laboratory for their technical support. The DFT calculations were performed using Pacific Northwest National Laboratory (PNNL) Research Computing and the Environmental Molecular Sciences Laboratory (EMSL), a national scientific user facility sponsored by DOE's Office of Biological and Environmental Research and located at PNNL in Richland, WA. PNNL is a multiprogram national laboratory operated for

the DOE by Battelle Memorial Institute under Contract DE-AC05-76RL01830.

References

1 D. S. Hall, D. J. Lockwood, C. Bock and B. R. MacDougall, *Proc. R. Soc. A*, 2015, **471**, 20140792.
2 Y. Lv, S. Huang, Y. Zhao, S. Roy, X. Lu, Y. Hou and J. Zhang, *Appl. Energy*, 2022, **305**, 117849.
3 P. Sahoo and S. K. Das, *Mater. Des.*, 2011, **32**, 1760–1775.
4 H. H. Pariser, N. R. Backeberg, O. C. M. Masson and J. C. M. Bedder, *J. South. Afr. Inst. Min. Metall.*, 2018, **118**, 563–568.
5 D. Zhou, X. Guo, Q. Zhang, Y. Shi, H. Zhang, C. Yu and H. Pang, *Adv. Funct. Mater.*, 2022, **32**, 2107928.
6 T. K. Ying, X. P. Gao, W. K. Hu, F. Wu and D. Noréus, *Int. J. Hydrogen Energy*, 2006, **31**, 525–530.
7 R. Basuhi, K. Bhuwalka, E. A. Moore, I. Diersen, R. H. Malik, E. Young, R. G. Billy, R. Stoner, G. Ceder, D. B. Müller, R. Roth and E. A. Olivetti, *Joule*, 2024, **8**, 2960–2973.
8 K. Zhao, F. Gao and Q. Yang, *J. Sustain. Metall.*, 2022, **8**, 37–50.
9 P. Meshram and B. D. Pandey, *Miner. Process. Extr. Metall. Rev.*, 2019, **40**, 157–193.
10 P. Lampropoulou, P. Petrounias, P. P. Giannakopoulou, A. Rogkala, N. Koukouzas, B. Tsikouras and K. Hatzipanagiotou, *Minerals*, 2020, **10**, 406.
11 A. J. Adewumi and T. A. Laniyan, *Hum. Ecol. Risk Assess.*, 2021, **27**, 307–326.
12 M. Petranikova, I. Herdzik-Koniecko, B.-M. Steenari and C. Ekberg, *Hydrometallurgy*, 2017, **171**, 128–141.
13 P. B. Kelemen, N. McQueen, J. Wilcox, P. Renforth, G. Dipple and A. P. Vankeuren, *Chem. Geol.*, 2020, **550**, 119628.
14 X. Lu, K. J. Carroll, C. C. Turvey and G. M. Dipple, *Appl. Geochem.*, 2022, **140**, 105285.
15 R. M. Santos, A. Van Audenaerde, Y. W. Chiang, R. I. Iacobescu, P. Knops and T. Van Gerven, *Metals*, 2015, **5**, 1620–1644.
16 Z.-Y. Hseu and Z.-S. Chen, in *Nickel in Soils and Plants*, ed. C. Tsadilas, J. Rinklebe and M. Selim, 2018, pp. 181–198.
17 A. A. Olajire, *J. Pet. Sci. Eng.*, 2013, **109**, 364–392.
18 F. Wang, D. Dreisinger, M. Jarvis, T. Hitchins and L. Trytten, *Chem. Eng. J.*, 2021, **406**, 126761.
19 F. Wang and D. Dreisinger, *Proc. Natl. Acad. Sci. U. S. A.*, 2022, **119**, e2203937119.
20 Y. Wang, C. Alexakos, T. J. Zaidman, J. Houghton, Z. Xie, D. A. Fike and Y.-S. Jun, *J. Phys. Chem. C*, 2025, **129**, 8570–8581.
21 V. Prigiobbe and M. Mazzotti, *Chem. Eng. J.*, 2013, **223**, 755–763.
22 M. Hänchen, V. Prigiobbe, R. Baciocchi and M. Mazzotti, *Chem. Eng. Sci.*, 2008, **63**, 1012–1028.
23 T. Isaacs, *Mineral. Mag. J. Mineral. Soc.*, 1963, **33**, 663–678.
24 K. D. Oh, H. Morikawa, S. I. Iwai and H. Aoki, *Am. Mineral.*, 1973, **58**, 1029–1033.
25 H. S. Santos, H. Nguyen, F. Venâncio, D. Ramteke, R. Zevenhoven and P. Kinnunen, *Inorg. Chem. Front.*, 2023, **10**, 2507–2546.
26 D. W. Kohls and J. L. Rodda, *Am. Mineral.*, 1966, **51**, 677–684.
27 G. M. Biggar, *Mineral. Mag.*, 1969, **37**, 299–300.
28 E. H. Nickel, J. F. M. Clout and B. J. Gartrell, *Mineral. Rec.*, 1994, **25**, 283–293.
29 R. Chulia-Jordan, D. Santamaria-Perez, A. Otero-de-la-Roza, J. Ruiz-Fuertes, T. Marqueño, O. Gomis, S. MacLeod and C. Popescu, *J. Phys. Chem. C*, 2020, **124**, 19781–19792.
30 K. Sawchuk, R. Kamat, C. McGuire and A. Kavner, *Phys. Chem. Miner.*, 2021, **48**, 7.
31 L. Friberg, G. F. Nordberg and V. B. Vouk, *Handbook on the Toxicology of Metals*, Elsevier/North-Holland Biomedical Press, Amsterdam, 1979.
32 D. Lee, Q. X. Xia, J. M. Yun and K. H. Kim, *Appl. Surf. Sci.*, 2018, **433**, 16–26.
33 C. Cheng, F. Chen, Y. Cheng and G. Lai, *Dalton Trans.*, 2022, **51**, 6832–6838.
34 M. K. Seguin, *Can. Mineral.*, 1973, **12**, 26–32.
35 S. Farsang, R. N. Widmer and S. A. T. Redfern, *Am. Mineral.*, 2021, **106**, 581–598.
36 Z. Liu, Y. Liu, Y. Zhong, L. Cui, W. Yang, J. M. Razal, C. J. Barrow and J. Liu, *J. Power Sources*, 2021, **484**, 229288.
37 Z. Lu, K. Zhao, H. Guo, L. Duan, H. Sun, K. Chen and J. Liu, *Small*, 2024, **20**, 2309814.
38 M. Tian, Y. Zhong, D. Fu, Z. Liu, L. Cui and J. Liu, *Adv. Sustainable Syst.*, 2022, **6**, 2100357.
39 C. Sandford, M. A. Edwards, K. J. Klunder, D. P. Hickey, M. Li, K. Barman, M. S. Sigman, H. S. White and S. D. Minteer, *Chem. Sci.*, 2019, **10**, 6404–6422.
40 S. Mahovic Poljacek, D. Risovic, T. Cigula and M. Gojo, *J. Solid State Electrochem.*, 2012, **16**, 1077–1089.
41 L. Zhao, Y. Li, M. Yu, Y. Peng and F. Ran, *Adv. Sci.*, 2023, **10**, 2300283.
42 X. Yi, C. Kirk and N. Robertson, *Carbon Neutrality*, 2024, **3**, 39.
43 T. Ajayi, J. S. Gomes and A. Bera, *Pet. Sci.*, 2019, **16**, 1028–1063.
44 P. Aliprandini, M. M. Jiménez Correa, J. A. Soares Tenório and D. C. R. Espinosa, *Influence of Metallic Impurities on Solvent Extraction of Cobalt and Nickel from a Laterite Waste Liquor*, REWAS 2019, Springer International Publishing, *Cham*, 2019, pp. 137–142.
45 G. Kresse and J. Hafner, *Phys. Rev. B: Condens. Matter Mater. Phys.*, 1993, **47**, 558–561.
46 G. Kresse and J. Hafner, *Phys. Rev. B: Condens. Matter Mater. Phys.*, 1994, **49**, 14251–14269.
47 G. Kresse and J. Furthmüller, *Phys. Rev. B: Condens. Matter Mater. Phys.*, 1996, **54**, 11169–11186.
48 G. Kresse and J. Furthmüller, *Comput. Mater. Sci.*, 1996, **6**, 15–50.
49 P. E. Blöchl, *Phys. Rev. B: Condens. Matter Mater. Phys.*, 1994, **50**, 17953–17979.
50 G. Kresse and D. Joubert, *Phys. Rev. B: Condens. Matter Mater. Phys.*, 1999, **59**, 1758–1775.

51 J. P. Perdew, K. Burke and M. Ernzerhof, *Phys. Rev. Lett.*, 1996, **77**, 3865–3868.
52 J. P. Perdew, K. Burke and M. Ernzerhof, *Phys. Rev. Lett.*, 1997, **78**, 1396.
53 S. Grimme, J. Antony, S. Ehrlich and H. Krieg, *J. Chem. Phys.*, 2010, **132**, 154104.
54 C. Adamo and V. Barone, *J. Chem. Phys.*, 1999, **110**, 6158–6170.
55 S. L. Dudarev, G. A. Botton, S. Y. Savrasov, Z. Szotek, W. M. Temmerman and A. P. Sutton, *Phys. Status Solidi A*, 1998, **166**, 429–443.
56 M. Sassi and S. N. Kerisit, *ACS Earth Space Chem.*, 2024, **8**, 1027–1038.